Bridgman Crystal Growth of an Alloy with Thermosolutal Convection under Microgravity Conditions[§]

James E. Simpson, Suresh V. Garimella[¶]
School of Mechanical Engineering
Purdue University
West Lafayette, Indiana 47907-1288
Phone: (765) 494-5621; Fax: (765) 494-0539
sureshg@ecn.purdue.edu

Henry C. de Groh III
NASA Glenn Research Center
Cleveland, Ohio 44135

Reza Abbaschian
Department of Materials Science and Engineering
University of Florida
Gainesville, Florida 32611

ABSTRACT

The solidification of a dilute alloy (bismuth-tin) under Bridgman crystal growth conditions is investigated. Computations are performed in two dimensions with a uniform grid. The simulation includes the species concentration, temperature and flow fields, as well as conduction in the ampoule. Fully transient simulations have been performed, with no simplifying steady state approximations. Results are obtained under microgravity conditions for pure bismuth, and for Bi-0.1 at.%Sn and Bi-1.0 at.%Sn alloys, and compared with experimental results obtained from crystals grown in the microgravity environment of space. For the Bi-1.0at.%Sn case the results indicate that a secondary convective cell, driven by solutal gradients, forms near the interface. The magnitude of the velocities in this cell increases with time, causing increasing solute segregation at the solid/liquid interface. The concentration-dependence of the melting temperature is incorporated in the model for the Bi-1.0 at.%Sn alloy. Satisfactory correspondence is obtained between the predicted and experimental results in terms of solute concentrations in the solidified crystal.

---

§ Submitted for possible publication in *ASME Journal of Heat Transfer*, October 1998 and in revised form, April 25, 2000

¶ Associate Professor, ***author to whom correspondence should be addressed***

NOMENCLATURE

c_p specific heat at constant pressure

C species concentration

D species diffusion coefficient

f volume fraction

g mass fraction

$\tilde{g}$ acceleration due to gravity

Gr Grashof number, $g\beta_T(T_H-T_C)H^3/\nu^2$

Gr_s solutal Grashof number, $g\beta_c C_0 H^3/\nu^2$

h ampoule thickness (outside radius - inside radius)

h_0 reference enthalpy = ? H/ρ

H ampoule diameter; reference length

k thermal conductivity

k_p segregation coefficient

L length of simulation domain

L_A translating zone length

Le Lewis number, a/D

Pr Prandtl number, ν/a

t time

T temperature

u, v velocities in x and y directions

Greek Symbols

a thermal diffusivity

ß expansion coefficient

? T temperature difference, $T_H - T_C$

? H enthalpy of freezing

ν kinematic viscosity

? radial segregation, $(C_{max} - C_{min})/C_{average}$

? density

Subscripts

0 initial condition

C cold furnace temperature condition

H hot furnace temperature condition

L liquid

m at solidification front

S solid

w ampoule wall

Superscripts

~ vector

* reference quantity

INTRODUCTION

The synthesis of advanced materials, especially for electronics and biomedical applications, demands high-quality crystals. The compositional uniformity (and hence the quality) of such crystals can be profoundly influenced by the transport phenomena which occur in the melt during solidification. The primary transport mechanism causing these deleterious effects is natural convection. The low-gravity environment of space offers an opportunity to suppress the strength of this natural convection. Hence there is a great deal of interest in the study of directional solidification of crystals in space.

The MEPHISTO project (Abbaschian et al., 1992) is a collaborative program of space experiments aimed at understanding the fundamental processes involved in crystal growth. The space-borne experimental apparatus is a Bridgman-type furnace with an isothermal hot zone, an isothermal chill zone, and an insulated gradient zone. The furnace contains three ingots of Bi-Sn or Sn-Bi binary alloy inside fused silica ampoules with a maximum 6 mm inner diameter and a 10 mm outer diameter. All three samples are solidified simultaneously under identical thermal conditions. After flight, the samples are extracted and analyzed. Four MEPHISTO space experiments have taken place; the most recent, MEPHISTO-4, flew in November 1997. The MEPHISTO-2 and -4

experiments examined the faceted solidification of bismuth doped with tin (Bi-Sn).

The experimental data from the MEPHISTO-2 mission experiments (with a Bi-0.1 at.% Sn alloy) resulted in a greater understanding of the dominant role of interface kinetics on morphological stability. Stability phenomena were observed that had not been previously predicted by theory or measured in terrestrial experiments (Abbaschian, 1996). The MEPHISTO-4 experiments built on to the previous results, and used a Bi-1.0 at.% Sn alloy.

The MEPHISTO project includes a program of computational modeling of the crystal growth process. In particular, the role of convection, which is crucial to a complete understanding of the process, is to be investigated. Since accurate experimental determination of convection in metallic melts is very difficult to achieve, due to the opacity and chemical reactivity of the melts, convective levels are determined numerically. Furthermore, the computational models themselves are to be improved by a process involving prediction of, and comparison with, the experimental results. The aim of this procedure is to develop effective *fully transient* computer simulations of fluid flow related effects. Previous computations of Bridgman growth had been limited to steady-state growth in succinonitrile, a widely used transparent phase change material with properties analogous to metallic materials (Yao and de Groh, 1993; de Groh and Yao, 1994).

Convection effects at microgravity levels were modeled by means of a transient, 2D FIDAP finite-element model by Yao et al. (1997). A fixed-grid approach was adopted, with the enthalpy method being employed to model the phase change. Temporal averaging was used for the apparent heat capacity in the discretized equations. Due to computational difficulties introduced by the small partition coefficient for Bi-Sn, the presence of solute was ignored in Yao et al. (1997). Preliminary scaling arguments by de Groh and Nelson (1994) implied that solutal convection effects on solute segregation may be significant. However, only recently has it been possible to include solutal

convection into numerical simulations involving phase change for MEPHISTO-4. This was due to the difficulties concerning convergence with front-tracking methods as well as those imposed by the low partition coefficient for Bi-Sn (Yao et al., 1995; Yao et al., 1997).

Many simulations of Bridgman crystal growth processes, both under terrestrial and microgravity conditions, are available in the literature. The majority of these simulations can be classified as *pseudo steady state* models. The key assumption in such models is that a "steady-state" mode of alloy solidification exists, i.e. the concentration of the dopant in the solid which forms at the interface is equal to the initial dopant concentration in the liquid (Kurz and Fisher, 1989). Such models vary in complexity from simple 2D analyses that consider the interface to be flat (Alexander et al., 1989; Yao et al., 1995; Simpson et al., 1998a) to much more complex formulations that are able to handle interface curvature and wall conduction (Adornato and Brown, 1987) and fully 3D simulations (Liang and Lan, 1996). However, because of the low partition coefficient for Bi-Sn alloys, a steady-state mode of solidification is never achieved during the MEPHISTO experiments. Thus pseudo steady state models are not appropriate; recently developed fully transient simulations, such as those of Simpson and Garimella (2000) and Timchenko et al. (2000) need to be employed and improved in order to faithfully model this process.

The computational modeling presented in this paper is intended to examine the effects of thermosolutal natural convection on the MEPHISTO-4 solidification experiments. This will be achieved using a *fully transient* 2D model, which includes most of the effects of binary alloy solidification, convection driven by both thermal and solutal gradients, distinct thermal properties in the solid and liquid phases and the effects of interface curvature. Compared to Simpson et al. (1998b), the solution scheme used in this work is improved in terms of the following aspects. Conduction through the ampoule wall is considered. The dependence of melting temperature on

concentration is included for the richer alloy. It must be stressed that for the growth rates and applied thermal gradients encountered during the highly controlled directional solidification experiments modeled in this paper, the liquid/solid interface was experimentally found to be *stable* and *non-dendritic* like that for a pure metal. Consequently, the solid/liquid interface modeled in our numerical analysis is also stable and non-dendritic.

MATHEMATICAL FORMULATION

The problem under consideration is the directional solidification of a binary alloy by the Bridgman process, as shown schematically in Fig. 1. The gravity vector is perpendicular to the furnace axis (horizontal Bridgman growth configuration). The melt region is considered to be a viscous Newtonian fluid subject to thermosolutal convection. Thermophysical properties are considered as constant but distinct for the solid and liquid phases. Density variations are considered to be subject to the Boussinesq approximation. The equation for conservation of momentum and mass are

$$\frac{\partial \tilde{u}}{\partial t} + (\tilde{\nabla} \times \tilde{u}) \times \tilde{u} = -\beta_T (T - T_C)\tilde{g} - \beta_C (C - C_0)\tilde{g} - \frac{\tilde{\nabla} P}{\rho_0} + \nu \nabla^2 \tilde{u} \tag{1}$$

$$\tilde{\nabla} \cdot \tilde{u} = 0 \tag{2}$$

For calculating nondimensional constants (such as thermal Rayleigh number, *Ra*) the ampoule inside diameter H is selected to be the reference length. The characteristic time and velocity become t^* $(= H^2/\alpha)$ and v^* $(= H/t^* = \alpha/H)$.

The governing equation for the conservation of energy is

$$A(T, C_L)\frac{\partial T}{\partial t} + \rho c_{pL} \tilde{\nabla} \cdot (\tilde{u} T) = \tilde{\nabla} \cdot (k \tilde{\nabla} T) + B(T, C_L) \tag{3}$$

It will be seen below that effective heat capacity A and source term B may be specified in this way

for calculating phase-change. An initial temperature equal to T_H is applied throughout the flow field. The temperatures at the $x = 0$ and $x = L$ walls are set to be T_H and T_C, respectively.

The thermal boundary conditions along $y = \bullet\ (H/2 + h)$ are a function of time and are shown schematically in Fig. 1. There is a translating zone (considered an "adiabatic" zone if the temperature profile is unknown) between the hot and cold regions of the furnace, in which the temperature linearly increases from the cold furnace temperature to the hot furnace temperature. The melting temperature of the material occurs somewhere within this zone, which translates with time at a constant x-velocity, known as the *translation velocity*, u_t. This is what facilitates the directional growth of the crystal. Defining the x location where the translating zone meets the cold furnace temperature zone to be at $x_A(t)$, the boundary condition for temperature may be expressed as

$$y = \pm\left(\frac{H}{2} + h\right): \quad T = \begin{cases} T_C, & x < x_A(t) \\ T_C + \Delta T \dfrac{x - x_A(t)}{L_A}, & x_A(t) \le x \le (x_A(t) + L_A) \\ T_H, & (x_A(t) + L_A) < x \end{cases} \tag{4}$$

In principle, the solution of the energy equation (3) coupled with the solution of the momentum and mass conservation equations (1 and 2) would yield the temperature and velocity distribution throughout the simulation domain. However, the problem of modeling the physics of the propagation of the solidification front and determining its location remains to be addressed. We choose to do this by employing the phase-transformation model of Zeng and Faghri (1994). In this model, apparent heat capacity A and source term B are given as

$$A(T,C_L) = \rho c_p + a(T,C_L)\frac{\partial f_L}{\partial T}$$

$$B(T,C_L) = -\tilde{\nabla}\cdot(\rho h_0 \tilde{u}) + \tilde{\nabla}\cdot\left[\rho f_S (h_0 + (c_{pL} - c_{pS})T)\tilde{u}_S\right] - a(T,C_L)\frac{\partial f_L}{\partial C_L}\frac{\partial C_L}{\partial t}$$

$$a(T,C_L) = \rho\left[(c_{pL} - c_{pS})T + \frac{(\rho_L - \rho_S)c_p T + \rho_L h_0}{\rho_L - f_L(\rho_L - \rho_s)}\right] \qquad (5a)$$

$$c_p = c_{pL} g_L + c_{pS} g_S$$

$$\rho = \rho_S f_S + \rho_L f_L$$

For the present study, the density of each phase is assumed to be equal, and there is no dispersion of solid phase moving in the liquid. For the results shown where the melting temperature is considered dependent on concentration, the full expressions for A and B (Eq. 5a) simplify to become:

$$A(T,C_L) = \rho c_p + a(T)\frac{\partial f_L}{\partial T}$$

$$B(T,C_L) = -a(T)\frac{\partial f_L}{\partial C_L}\frac{\partial C_L}{\partial t} \qquad (5b)$$

$$a(T) = \rho\left[(c_{pL} - c_{pS})T + h_0\right]$$

For the pure bismuth and dilute alloy results, concentration-dependence on temperature is neglected, and the expressions for A and B simplify further to

$$A(T) = \rho c_p + a(T)\frac{\partial f_L}{\partial T}$$

$$B(T) = 0 \qquad (5c)$$

$$a(T) = \rho\left[(c_{pL} - c_{pS})T + h_0\right]$$

The equation for conservation of solute throughout the computational domain is

$$\frac{\partial C_L}{\partial t} + \tilde{\nabla}\cdot(\tilde{u}C_L) = D\nabla^2 C_L + S(T,C_L) \qquad (6)$$

This equation is analogous to the energy equation. We impose an initial solute concentration throughout the solution domain. At the boundaries no solute may exit the solution domain. Thus,

$$t = 0 \qquad C_L = C_0$$

$$x = 0, L \qquad \bullet C_L/\bullet x = 0 \qquad (7)$$

$y = 0, H \qquad \bullet C_L/\bullet y = 0$

Again, in principle, solution of equation (6) along with energy equation (4) and the fluid velocities all subject to the relevant boundary and initial conditions is enough to determine the solute, temperature and velocity values throughout the solution domain. However, the more general problem involving phase change demands that solute redistribution at the advancing solid/liquid interface be addressed. At the interface, new solid material forms at a concentration lower than at the adjacent liquid, in accordance with the partition coefficient (Kurz and Fisher, 1989):

$$C_S^* = k_p C_L^* \tag{8}$$

For the Bi-Sn system under consideration in this work, the partition coefficient k_p has a value of 0.029. This small value indicates that the solid forms at a concentration very poor in solute, and thus there is rapid and significant build-up of solute in the liquid region ahead of the interface. Source term S accounts for solute rejection at the interface into the bulk fluid resulting from the effect of the solid material forming at the lower concentration. Following the work of Swaminathan and Voller (1997) and Voller et al. (1989) source term S may be written as the differential

$$S(T, C_L) = \frac{\partial (f_L C_L)}{\partial t} + k_p C_L \frac{\partial f_S}{\partial t} \tag{9}$$

NUMERICAL ANALYSIS

The numerical scheme is explained in detail in Simpson and Garimella (1998, 2000); only salient details are provided here. The computational domain is primarily discretized using regularly spaced finite difference mesh points. Superimposed on this grid are finite volumes which are used for the solution of the energy and species concentration equations. The finite volume centers are staggered with respect to the finite difference mesh point locations. Vorticity, velocity and vector potential are

calculated at the finite difference mesh points. Temperature and solute concentration are evaluated using the finite volumes.

For solving velocities, the vorticity-streamfunction representation of the Navier-Stokes and continuity equations (1 and 2) is used. The numerical approach applied here is modified from a program (Timchenko et al., 1997) written for the solution of natural convection in a rectangular cavity. The essential details are that the discretized equation for the vorticity transport equation is solved using an Alternating Direction Implicit scheme (Samarskii and Andreyev, 1963). The discretized equation for streamfunction is solved using the conjugate gradient method. Once the values of streamfunction are known, the nodal velocities can be determined. Boundary conditions are explicitly applied on the advancing solid/liquid interface which is arbitrarily oriented and so the boundary conditions require special handling. The location and slope of the interface is calculated using a Hirt and Nichols (1981) type front reconstruction; the boundary conditions may then be applied once the slope and position of the front are known.

The energy (4) and solute conservation (6) equations are discretized using the finite volume mesh, with an upwind scheme incorporated for the treatment of convective heat fluxes. The discretized equations are solved using iterative solvers - either Gauss-Seidel iteration or Stone's strongly implicit procedure (Ferziger and Peric, 1996). For the general case where melting temperature is dependent on interface concentration, the concentration and energy equations are highly coupled and are solved simultaneously.

RESULTS AND DISCUSSION

Validation

A grid-independence study was undertaken to determine the appropriate spatial and temporal

discretization scheme to be used. This study involved examining the solution fields from a test matrix of simulations performed using four different discretization schemes. Four mesh sizes of increasing spatial and temporal refinement were examined. The mesh selected on the basis of this grid independence study was a regularly spaced 300• 35 mesh, with 25 of the 35 y-direction cells being in the sample and the remaining 10 in the ampoule walls. The time step size was ? t = 0.1338 s. Detailed results from the grid-independence study, including plots of key field variables, are available in Simpson and Garimella (2000). The key points are:

- The thermal field results were almost identical for all four meshes.
- The difference between the velocities predicted by the mesh adopted in this study and those from a finer mesh was less than 3%.
- Particular attention was given to the concentration values in the solidified material. The concentrations in the solid are completely dependent on the solutal, thermal and flow fields in the melt, and so, are very sensitive to any changes in these fields. Concentration traces in the solid for the mesh employed in this study had a maximum discrepancy of only 3.2% (with the majority of values being less than 1%) compared to results at the finer mesh.

These results make it clear that (a) all the field variables converge to a single result as the mesh becomes increasingly fine, and (b) the mesh employed in this work is fine enough to obtain meaningful results while keeping computational costs reasonable.

Pure Bismuth

Simulations for the Bridgman crystal growth of pure bismuth were performed. The cold and hot furnace temperatures were T_C = 50• C and T_H = 700• C respectively. Thermophysical properties from Yao et al. (1995) were used, and are shown in Table 1. Key nondimensional parameters

describing thermal transport are Gr = 113.6 and Pr = 0.01144. For this pure Bismuth case, there is no solute, so the dilute model for phase chance (Eq. 5c) was used.

In order to start each of the crystal growth simulations, the following procedure was carried out. The initial position of the translating zone was flush with the x = 0 wall. This zone is immobilized for the first 3,000 time steps. During this time, the velocity and concentration field solution schemes are switched off while solid rapidly chills in the portion of the translating zone which is lower than the melting temperature. This new state is then taken to be at time t = 0. After this, simulations proceed with the entire solution scheme enabled and the insulated zone moving at the translation velocity u_t.

Figure 2(a) shows a plot of velocity vectors and isotherms after 3,000 s have elapsed. Isotherms are shown in the ampoule wall as well as in the liquid and solid bismuth. The thick line at x • 16 mm represents the solid/liquid interface. The dominant feature of this plot is the counter-clockwise convective cell in the translating zone (16 < x < 40 mm). For clarity, velocity vectors are plotted on every *third* mesh point in the x-direction in this figure. The maximum velocity in this convective cell is 3.47 μm/s at (24.75, • 1.8 mm). The ratio of this velocity to the translation velocity, u_t, is 1.03, which compares to the value of 1.12 found from the finite-element, variable-property simulation of the same process by Yao et al. (1997). Velocities in the negative y-direction at the interface are constrained and concentrated by the presence of the solid whereas velocities in the positive y-direction at the opposite (hot) end of the translating zone are much more diffuse.

The other main feature of this plot is the isotherms throughout the solution domain. On the outside edge of the ampoule, the (imposed) linear temperature profile within the translating zone is witnessed by the regularly spaced isotherms on the outer edge. In the low-conductivity ampoule the isotherms are dramatically distorted, and the thermal field on the inside of the ampoule wall differs

from that imposed on the outside. For x • 24 mm, the temperature in the ampoule is greater than the applied temperature (the isotherms distort sharply to the left); for x • 24 mm, the converse is true. In the bismuth region the isotherms exhibit the same trend, and have a gentle, crescent-shaped curvature. The isotherms and the interface appear to be symmetric about the centerline (y = 0) and thus have not been influenced by convective transport in the melt. The solid-liquid interface, which is an isotherm, is discernibly curved such that the solid is concave. The total deflection of the interface is about 0.5 mm which compares to a value of ~0.46 mm found in Yao et al. (1997). This curvature is primarily a result of the difference in thermophysical properties for the solid and liquid phases. Translation of the thermal boundary condition also contributes slightly to this effect.

Figures 2(b) and 2(c) are plots of velocity vectors and isotherms at 6,000 and 9,000 s, respectively. The progression of the translating zone (and thus of the solidification front) is obvious from these figures. After 6,000 s, the front is at x • 26 mm, and the nature of the convective motions is unchanged. The magnitude of the maximum velocities at these later times is identical to that at the previous time (Fig. 2a). This indicates that end effects are not influencing the results. The curvature of the interface also remains the same.

Bi• 0.1 at.% Sn alloy (MEPHISTO-2)

The growth of a Bi• 0.1 at.% Sn (0.08185 vol.% Sn) alloy was considered next. The velocity, thermal and solute fields were solved subject to the dilute alloy model (Eq. 5c), and the dimensionless parameters for solute transport are Gr_s = 0.349 and Le = 3074. Simulations were performed using the same spatial discretization and time step as for pure bismuth.

The nature of the convective flow for this alloy (results not shown) is similar to that for pure bismuth. A single counter-clockwise thermally driven convective cell dominates the domain. The

maximum u-velocity is slightly less than for pure bismuth, and is at the same location. However, the magnitude of the maximum v-velocity is • 1.77 μm/s at (17.75, 0 mm) acting in the negative y direction, which is lower in magnitude than for pure bismuth (• 1.87 μm/s). Solute rejected at the interface acts to oppose the thermally driven convective motion, resulting in retarded velocities near the interface. The thermal field is not distorted by the action of convection. As time progresses to 6,000 and 9,000 s, the maximum v-velocity decreases to • 1.72 μm/s and • 1.65 μm/s respectively, as a result of continuing solute rejection at the interface.

Traces of solute concentration across the height of the solidified alloy in the domain are shown in Fig. 3. Three different x-locations (16.18, 26.30, 36.41 mm) are considered, corresponding to the location of the interface at y = 0 at times of 3,000, 6,000 and 9,000 s, respectively. To aid in visualizing the influence of convection, results for a simulation involving diffusion only (no convection) are superimposed on this plot. Note that these pure diffusion results indicate that significant radial segregation arises due to interface curvature (see Adornato and Brown, 1987; Liang and Lan, 1996) such that the solute concentrations at the centerline are larger than those at the edges. The level of curvature-induced radial segregation remains almost constant, with values of ? = 29.1% (based on the mean concentration) at x = 16.18 mm and 29.4% at x = 26.30 and 36.41 mm. The inclusion of convection into the calculations causes the following effects. Solute levels are increased for low values of y and decreased for higher values of y. The y-location for the maximum solute concentration is also shifted from the centerline to y = • 1.23 mm for all the traces. This is a consequence of the convective flow sweeping solute Adown@ the interface in the direction of decreasing y and away from the interface in the direction of increasing x. The maximum values for solute concentration are C_{max}/C_0 = 0.30, 0.50, 0.65 for the traces at x = 16.18, 26.30 and 36.41 mm, respectively. The radial segregation values increase slightly from ? = 50.1% at x = 16.18 mm to

56.3% at x = 36.41 mm.

Traces of solute concentrations in the solid *and* melt at the different times are shown in Fig. 4. These traces run longitudinally along the ampoule for three different heights of y = • 2.88, 0 and 2.88 mm. Note that the interface location on the centerline (y = 0) trace lags slightly behind the value for the other traces since the interface is curved. Solute build-up near the interface, and the exponential profile characteristic of binary-alloy solute rejection (Smith et al., 1955) are clearly evident. The concentration at the centerline increases from $C/C_0 = 9.62$ at 3,000 s to 20.79 at 9,000 s. The impact of convection can also be seen in this plot. Warm, solute-poor fluid impinges on the top section of the interface. This fluid, cooled by the interface, falls toward the bottom wall and then returns to the bulk. This convective transport causes a thinner solute boundary layer and lower interface concentration value for y = 2.88 mm and, conversely, a thicker solute boundary layer and higher interface concentration value for y = • 2.88 mm. The interface concentrations along the centerline remain larger than those found at the periphery for all the times shown. This effect is due to interface curvature (see Fig. 3). The axial segregation in the solidified crystal is seen to increase with time; the radial segregation evident in Fig. 3 is also seen in Fig. 4.

For the low-concentration alloy, the solute concentration profiles are governed by solute rejection at the (curved) interface and by thermal convection only. The action of solutal convection is limited at these low concentrations. The velocity field indicates that thermal convection decreases slightly with time.

Bi• 1.0 at.% Sn alloy (MEPHISTO-4)

A richer alloy was simulated next. The initial liquid composition was taken to be at a uniform 1.0 at.% Sn (0.8185 vol.% Sn) increasing the value of Gr_s to 3.49. The dilute model (Eq. 5c) was

retained for this initial investigation; the validity of this is commented upon later.

Velocity vectors and isotherms at three different times are shown in Fig. 5. At 3,000 s (Fig. 5a) the velocities indicate a primary counter-clockwise convective cell in the translating zone, along with a weak secondary, clockwise cell driven by solute gradients adjacent to the interface. The two-cell convective motion is in contrast to that observed for pure bismuth and for the more dilute alloy. The maximum v-velocity in the secondary convective cell near the interface at (16.5, 0 mm) is 0.57 μm/s. The nature of the maximum velocities for this case is also different due to the higher levels of solute rejection and the presence of the secondary cell. The maximum u-velocity for this case is slightly lower than that for pure bismuth. The maximum v-velocity is identical to the value for pure bismuth but is located further from the interface (x = 19.25 versus x = 17.75 mm for the pure and Bi-0.1 at.% Sn cases).

At a later time (Fig. 5b), the secondary convective cell has increased in size and strength as solute - the driving force for this cell - continues to build up at the interface. The maximum v-velocity in the secondary convective cell near the interface at (27.00, 0.48 mm) is 1.75 μm/s. Later in the growth process (Fig. 5c), the front has advanced to x • 36 mm, and the secondary convective cell has become quite strong. The maximum v-velocity in the secondary cell (and in the domain) is 2.88 μm/s at (37.00, 0.36 mm).

Traces of solute concentration across the height of the solidified alloy, along with pure diffusion results, are shown in Fig. 6. This plot provides a stark contrast with the results shown for the more dilute alloy in Fig. 3; the formation and growth of the secondary cell causes segregation to occur in the opposite sense (such that concentration values near the top of the domain are higher than at the bottom). At x = 16.18 mm, the concentrations are close to those for pure diffusion; the maximum value is $C/C_0 = 0.28$ at y = 0.059 mm with a segregation value of ? = 28.9%. This serendipitous

result is a consequence of segregation arising from the influence of the secondary cell balancing the segregation caused by the thermally driven cell when solidification has proceeded to this location. At lower values of x ($t < 3{,}000$ s), segregation is such that the maximum value occurs at $y < 0$ (similar to the Bi-0.1 at.% Sn alloy result, see Fig. 3) while at higher values of x ($t > 3{,}000$ s) this maximum is shifted to a more positive y value. The traces at x = 26.30 and 36.41 mm show that increasing solutal convection leads to increasing radial segregation. The maximum values are C/C_0 = 0.51 and 0.75 with radial segregation levels of ? = 54.7 and 82.2%, respectively. This behavior is different from the case shown in Fig. 3, where the convective field remained almost steady with respect to the interface resulting in only a slight increase in segregation.

Figure 7 is a plot of longitudinal solute concentrations at domain heights of y =• 2.88, 0 and 2.88 mm for the Bi-1.0 at.% Sn case at the three different times. As for the case shown in Fig. 4 there is significant solute buildup, with liquid solute concentrations C/C_0 at the interface along the centerline being 9.70, 15.59 and 19.20, respectively. Note, however, that this corresponds to much higher concentrations than for the case shown in Fig. 4 due to the higher initial concentration C_0. Near the interface, the solute concentrations in the liquid are higher at y = 2.88 mm than at y =• 2.88 mm. Further from the interface, but still within the solute boundary layer, concentration increases with decreasing y. This is due to the interaction of the two convective cells. Close to the interface, the secondary cell circulates solute-rich material within the boundary layer, acting to accumulate solute-rich material in this region. Further from the interface (see Fig. 5), the primary convective cell influences the solute distribution, sweeping solute from the bottom of the domain into the bulk and thickening the solute boundary layer in this region. In general, the solute boundary layers are more compact than for the dilute alloy case at each corresponding time. Note that concentration values of this magnitude would be sufficient to lower the melting temperature of the alloy by a significant

amount (Simpson et al., 1998a). This implies that the constant melting temperature assumption made in these simulations is not valid. This effect will be addressed in the next subsection.

For the higher alloy concentrations, solutal convection plays a much larger role, as can be seen in the concentration profiles discussed above. As growth proceeds, the level of solutal convection grows, with a corresponding increase in radial segregation. The maximum concentration increases much more rapidly than the minimum value.

Figure 8 is a plot of *average* solute concentrations in the solid at 3,000, 6,000 and 9,000 s for both the dilute and rich alloy. Averaging is performed across the height of the solidified material (y = • 3 to 3 mm). For comparison purposes, average concentrations for the pure diffusion case as well as those calculated from an analytical expression for solid solute concentrations under 1D, pure diffusion growth conditions (Smith et al., 1955) are also shown. The pure diffusion results exhibit good agreement with the 1D analytical result; the largest difference between these results is 1.2% at 3,000 s. The lowest average solid concentrations are found for the dilute alloy (Bi-0.1 at.%Sn). After 3,000 s the dilute alloy concentration is 1.3% less than for pure diffusion. With time, this deficit increases to 2.2% after 6,000 s and 2.1% after 9,000 s. The average solute concentrations for the richer alloy (Bi-1.0 at.% Sn) lie between those found for the pure diffusion and Bi-0.1 at.% Sn results. These concentrations are 0.76, 1.2 and 1.7% lower than the pure diffusion values after 3,000, 6,000 and 9,000 s, respectively. For the dilute alloy, the single convective cell acts, on average, to increase the size of the solute boundary layer (Fig. 5) by transporting solute from the interface out into the melt (Fig. 3). This results in a corresponding decrease in the average solid concentration levels when compared to the pure diffusion case, for a given y-location. For the richer alloy, the solute boundary layers are shaped by a more complicated convection pattern (Fig. 6). In general, the boundary layers are more compact than for the dilute alloy case, resulting in slightly higher average

concentrations. The difference between the average concentration found for the pure diffusion and Bi-1.0 at.%Sn cases increases with increasing solutal convection levels.

Comparison with Experiment

An actual solidification process carried out during the MEPHISTO-4 space experiment was modeled using the rich-alloy model (Eq. 5b) which accounts for the effect of concentration-dependent melting temperature. The main difference in this simulation compared to those above is that the solidification cycle selected was conducted at a furnace translation rate of 11.997 μm/s for a duration of 334 seconds, resulting in a total furnace translation of 4 mm. The gravity level for this case was reduced to 1 μg, which is more typical of residual gravity levels during the experiment (de Groh and Nelson, 1994). Under these conditions, the process is diffusion-dominated although there is some discernible convection-induced segregation (Simpson and Garimella, 2000).

Figure 9 is a plot of concentration values along the centerline of the sample. The square symbols are experimental data points obtained via a post-flight microprobe analysis of the solidified sample **(REZA/HENRY: PLEASE PROVIDE A REFERENCE FOR THE POST-FLIGHT DATA REPORT)**. Although there is scatter in the experimental data, a clear trend of increasing concentration values can be discerned. The solidification process depicted starts at a location 143.5 mm along the ampoule; on Fig. 9, this location is taken as the origin $x = 0$ at $t = 0$. Then, in order to grow crystal from the melt, the furnaces are moved at a constant velocity. As the furnaces begin to move and new crystal is formed, solute begins to pile up at the interface. As the concentration at the interface increases, the local melting temperature decreases. Hence the front slowly "melts back" with respect to the furnaces and thus moves at a speed that is *slower* than the furnace translation velocity. After 334 seconds have elapsed, the furnaces have traversed 4 mm, however, the

solid/liquid interface has moved only 3.1 mm, and so only 3.1 mm of crystal is grown. The results from the numerical simulation, using the rich alloy model (Eq. 5b) that includes the effect of concentration-dependent melting temperature, are superimposed on this plot as the thick solid line. The experimental and numerical results are shown for a transverse location of y = 0. These results agree reasonably well with the experimental data both in terms of the predicted values of concentration and in terms of predicting the total amount of material grown. Results of a simulation using the dilute model (Eq 5c, no concentration-dependence of melting temperature) are also shown as a dashed line on the figure. This simulation clearly cannot handle the "melt back" of the interface and is therefore not able to predict the correct final location of the solid-liquid interface or accurate values of concentration.

The effect of the inclusion of concentration-dependent melting temperature in the calculations is to predict less net solute rejection into the liquid at a given time, since the front moves at an overall slower rate. If this concentration-dependence was incorporated into the results considered in Figs. 5, 6 and 7 for Bi-1.0 at.% Sn above, the primary differences would be twofold. First, less net solute would be rejected, so that the gradients in the liquid region near the interface would be less steep, resulting in lower levels of convection and hence lower levels of segregation at a given time. The other main effect would be to alter the shape of the interface slightly, such that it would be flatter in regions of higher liquid solute concentrations at the interface.

CONCLUSIONS

A series of fully transient simulations of horizontal Bridgman crystal growth under microgravity conditions have been performed. The pure bismuth simulation was found to agree reasonably well with a similar simulation of the process (Yao et al., 1997), in terms of the convection level and the interface curvature.

For the dilute alloy simulation (Bi-0.1 at.% Sn), a single dominant counter-clockwise convective cell is present for the entire duration of the process. As time proceeds, solute is rejected at the interface and the level of solute near the interface increases. Due to the presence of convection, radial solute segregation occurs with preferentially higher values at the bottom of the solid. The level of segregation increases slightly with time. The maximum values of concentration are small and so the assumption of constant alloy melting temperature is realistic.

For the richer alloy (Bi-1.0 at.% Sn), the convective field is much more complex. Higher levels of solute rejection at the interface cause higher levels of solutal convection. Initially, a single, thermally driven, counter-clockwise rotating cell is present. As time proceeds and solute accumulates at the interface, a secondary, solute-driven clockwise rotating cell develops. The effect of this convective pattern is to yield significant levels of segregation in the solute at the interface (and hence in the solid). This segregation is such that the values towards the top of the domain are highest. The higher values of concentration near the interface would result in a significant change in the melting temperature for the alloy. For this richer alloy, solute build-up is significant and so the concentration-dependence of the melting temperature becomes important.

Finally, simulations of Bridgman crystal growth in microgravity, incorporating the effects of a concentration-dependent melting temperature were performed. The results agree well with data obtained from the flight experiment. The combination of numerical simulations and experimental

data presented here has described the role of thermosolutal convection and solute partitioning during directional solidification.

Acknowledgements

Partial funding for this work from NASA (Coop. Agreement # NCC3-557) is gratefully acknowledged. JES was funded by a UW-Milwaukee Graduate School Fellowship. The insightful help of Dr. M. Yao of the Ohio Aerospace Institute is much appreciated. Professors G. de Vahl Davis and E. Leonardi and Dr. V. Timchenko of the University of New South Wales are thanked for kindly providing their code, FRECON3V, which was the basis for the velocity solution scheme used in this work.

REFERENCES

Abbaschian, R., Gokhale, A. B., Favier, J. J. and Coriell, S. R., 1992, In-Situ Monitoring of Crystal Growth Using MEPHISTO, NASA Science Requirements Document (SRD).

Abbaschian, R., 1996, In-Situ Monitoring of Crystal Growth Using MEPHISTO: Revised Science Requirements Document (RSRD) for the Re-flight of MEPHISTO aboard USMP-4.

Adornato, P. M. and Brown, R. A., 1987, Convection and segregation in directional solidification of dilute and non-dilute binary alloys, *J. Crystal Growth,* Vol. 80, pp. 155-190.

Alexander, J. I. D., Ouazzani, J. and Rosenberger, F., 1989, Analysis of the low gravity tolerance of Bridgman-Stockbarger crystal growth, *J. Crystal Growth,* Vol. 97, pp. 285-302.

de Groh III, H. C. and Nelson, E. S., 1994, On residual acceleration during space experiments, *Heat Transfer in Microgravity Systems*, ASME HTD-Vol. 290, pp. 23-33.

de Groh III, H. C. and Yao, M., 1994, Numerical and experimental study of transport phenomena in directional solidification of succinonitrile, *Transport Phenomena in Solidification*, ASME HTD-Vol 284, pp. 227-243.

Ferziger, J. H. and Peric, M., 1996, *Computational Methods for Fluid Dynamics,* Springer-Verlag.

Hirt, C. W. and Nichols, B. D., 1981, Volume of fluid (VOF) method for the dynamics of free boundaries, *J. Comp. Phys.,* Vol. 39, pp. 210-225.

Kurz, W. and Fisher, D. J., 1989, *Fundamentals of Solidification,* Trans Tech Publications.

Liang, M. C. and Lan, C. W., 1996, Three-dimensional convection and solute segregation in vertical Bridgman crystal growth, *J. Crystal Growth*, Vol. 167, pp. 320-332.

Samarskii, A. A. and Andreyev, V. B., 1963, On a high-accuracy difference scheme for an elliptic equation with several space variables, *USSR Comput. Math. and Math. Phys.,* Vol. 3, pp. 1373-1382.

Simpson, J. E. and Garimella, S. V., 1998, An investigation of the solutal, thermal and flow fields in unidirectional alloy solidification, *Int. J. Heat Mass Transfer*, Vol. 41, pp. 2485-2502.

Simpson, J. E., Yao, M., de Groh III, H. C. and Garimella, S. V., 1998a, Numerical modeling of solidification in space with MEPHISTO-4 (Part 2), NASA Technical Memorandum TM-1998-206630.

Simpson, J. E., Garimella, S. V., de Groh III, H. C. and Abbaschian, R., 1998b, Melt Convection

Effects in the Bridgman Crystal growth of an Alloy under Microgravity Conditions, *Procs. 7th AIAA/ASME Joint Thermophysics and Heat Transfer Conference*, Albuquerque, New Mexico, ASME HTD-Vol. 357-4, pp. 123-132.

Simpson, J. E., and Garimella, S. V., 2000, The influence of gravity levels on the horizontal Bridgman crystal growth of an alloy, *Int. J. Heat Mass Transfer*, Vol. 43, pp. 1905-1923.

Swaminathan, C. R. and Voller, V. R., 1997, Towards a general numerical scheme for solidification systems, *Int. J. Heat Mass Transfer*, Vol. 30, pp. 2859-2868.

Smith, V. G., Tiller, W. A. and Rutter, J. W., 1955, A Mathematical Analysis of Solute Redistribution During Solidification, *Canadian J. Phys*, Vol. 33, pp. 723-743.

Voller, V. R., Brent, A. D. and Prakash, C., 1989, The modelling of heat, mass and solute transport in solidification systems, *Int. J. Heat Mass Transfer*, Vol. 32, pp.1719-1731.

Timchenko, V., Chen, P. Y. P., Leonardi, E., de Vahl Davis, G. and Abbaschian, R., 2000, A computational study of transient plane front solidification of alloys in a Bridgman apparatus under microgravity conditions, *Int. J. Heat Mass Transfer*, Vol. 43, pp. 963-980.

Timchenko, V., Leonardi, E. and de Vahl Davis, G., 1997, FRECON3V User's Manual, University of New South Wales, School of Mechanical and Manufacturing Engineering, Report 1997/FMT/1, and FRECON3V Programmers Manual, Report 1997/FMT/2.

Yao, M. and de Groh III, H. C., 1993, Three-dimensional finite element method simulation of Bridgman crystal growth and comparison with experiments, *Num. Heat Transfer A*, Vol. 24, pp. 393-412.

Yao, M., de Groh III, H. C. and Abbaschian, R., 1997, Numerical modeling of solidification in space with MEPHISTO-4 (Part 1), *35th Aerospace Sciences Meeting and Exhibit*, Reno, NV, Paper AIAA 97-0449.

Yao, M., Raman, R. and de Groh III, H. C., 1995, Numerical simulation of heat and mass transport during space crystal growth with MEPHISTO, NASA Technical Memorandum 107015.

Zeng, X. and Faghri, A., 1994, Temperature-transforming model for binary solid–liquid phase-change problems part 1: mathematical modeling and numerical methodology, *Num. Heat Transfer B*, Vol. 25, pp. 467-480.

Table 1. Thermophysical Properties.

The properties (except the solutal diffusion coefficient D) for solid and liquid bismuth were evaluated at the mean solid and the mean liquid temperatures of 160.7 and 485.7• C, respectively. The solutal diffusion coefficient was evaluated at a position halfway into a typical solute boundary layer, since solute diffusion occurs mainly in this region. The reference density was considered to be equal for both phases.

Property	Units	Value
Reference density, $\bullet_0$	kg/m^3	10070
Thermal conductivity of the solid, k_S	W/mK	6.872
Thermal conductivity of the liquid, k_L	W/mK	14.66
Specific heat of the solid, c_{pS}	J/kgK	132.6
Specific heat of the liquid, c_{pL}	J/kgK	135.3
Enthalpy of freezing, • H	kJ/kg	52.3
Viscosity of the liquid, μ	Ns/m	$1.240 \times 10^{\bullet 3}$
Melting temperature, T_m	•C	271.3
Thermal expansion coefficient, $\bullet_T$	$K^{\bullet 1}$	$\bullet 1.25 \times 10^{\bullet 4}$
Thermal conductivity of the (fused silica) ampoule, k_w	W/mK	2.10
Density of the (fused silica) ampoule, $\bullet_w$	kg/m^3	2020
Specific heat of the (fused silica) ampoule, c_{pw}	J/kgK	1066.8
Partition (or segregation) coefficient, k_p	—	0.029
Diffusivity of liquid Sn in liquid Bi, D	m^2/s	$3.50 \times 10^{\bullet 9}$
Solutal expansion coefficient, $\bullet_C$	$(vol.\%)^{\bullet 1}$	• 0.305
Prandtl number, Pr	—	0.01144
Lewis number, Le	—	3074
Slope of liquidus line, m	K/(vol%)	-2.547

List of Figures

Fig. 1. Variation of the activation energy for creep, normalized by the activation energy for lattice self-diffusion, with the homologous temperature for several materials showing the probable dominance of dislocation core and lattice self-diffusion at intermediate and high temperatures, respectively [22].

Fig. 2. Dependence of the experimental activation energy for creep for (a) & (c) NaCl single crystals [40,41], (b) Cu [34] and (d) NiAl [46] on either the homologous temperature or the normalized stress. Note that E is the Young's modulus in (d). The horizontal broken lines represent the activation energies for lattice diffusion and pipe diffusion, Q_p, of the different species. Region I in (d) represents a low stress regime, whereas II and III represent the power-law and the exponential creep regimes, respectively. The experimental data are also compared with the predictions of pipe-to-lattice self-diffusion transition models [22], cross-slip [27,29] and obstacle-controlled [6] creep theories.

Fig. 3. Normalized creep rate vs. normalized stress plots for (a) f.c.c. metals compiled from the literature [15], (b) NaCl single crystals [47] and (b) NiAl [46] showing the transition from power-law to exponential creep.

Fig. 4 Effect of grain size on the compressive deformation behavior of (a) FeAl [49,50] and (b) & (c) as-cast and powder-metallurgy processed NiAl [48] showing grain size strengthening in intermetallic alloys at high temperatures.

Fig. 5 Creep substructures observed in the secondary creep regime in (a) pure Al [52], (b) NaCl single crystals [47], (c) NiAl [46] and (d) a $Ti_{47}Al_{51}Mn_2$ alloy [69].

Fig. 6 A simplified schematic diagram showing how an initially homogeneous distribution of dislocations could bifurcate into several possible dislocation substructures during deformation.

Fig. 7 Schematic plots demonstrating that the transient primary creep stages, A, B, C and D shown in (a) correspond to the structure-dependent (i.e. S_i) exponential curves in the normalized strain rate-normalized stress plot shown in (b).

Fig. 8 (a) Variation of creep strain, creep rate and the applied stress with time. A homogeneous distribution of dislocations is assumed to form as soon as plastic deformation commences, which is assumed to evolve to a mixture of light patches (i.e. recovered regions with a lower dislocation density), tangles and homogeneous dislocations as shown in (b) at the resolution limit. (c) Schematic showing the concept of "hard" and "soft" regions with respect to the light patches assumed by the model.

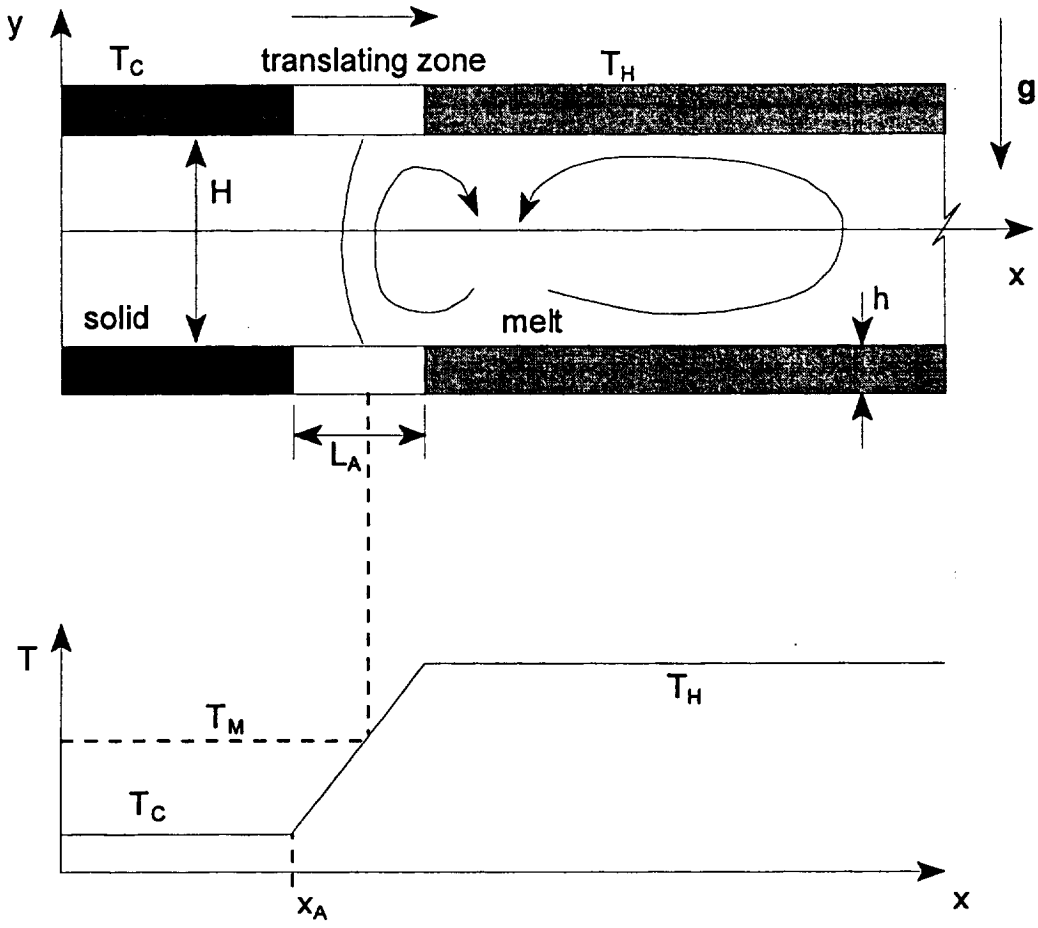

Simpson et al. Fig. 1

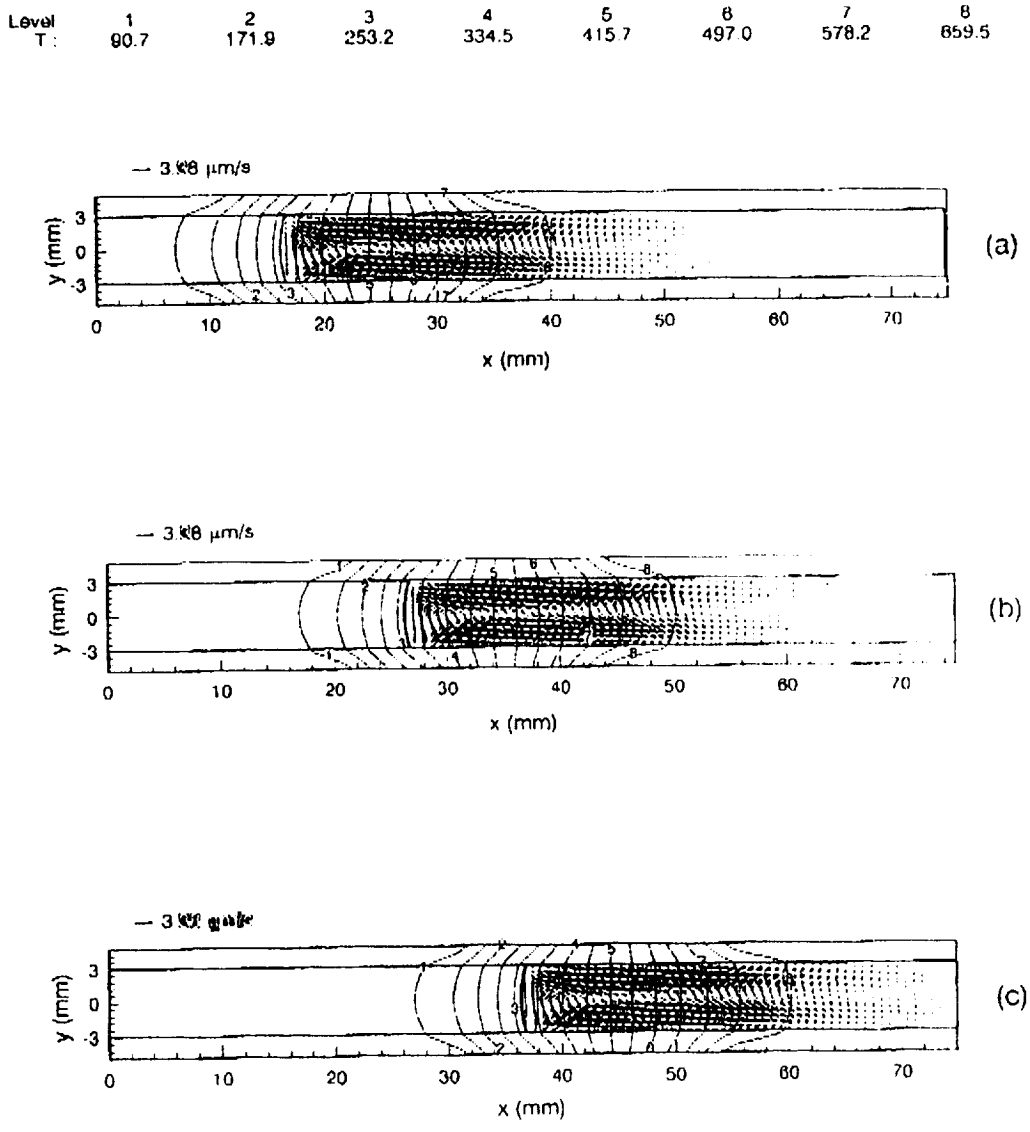

Simpson et al. Fig. 2

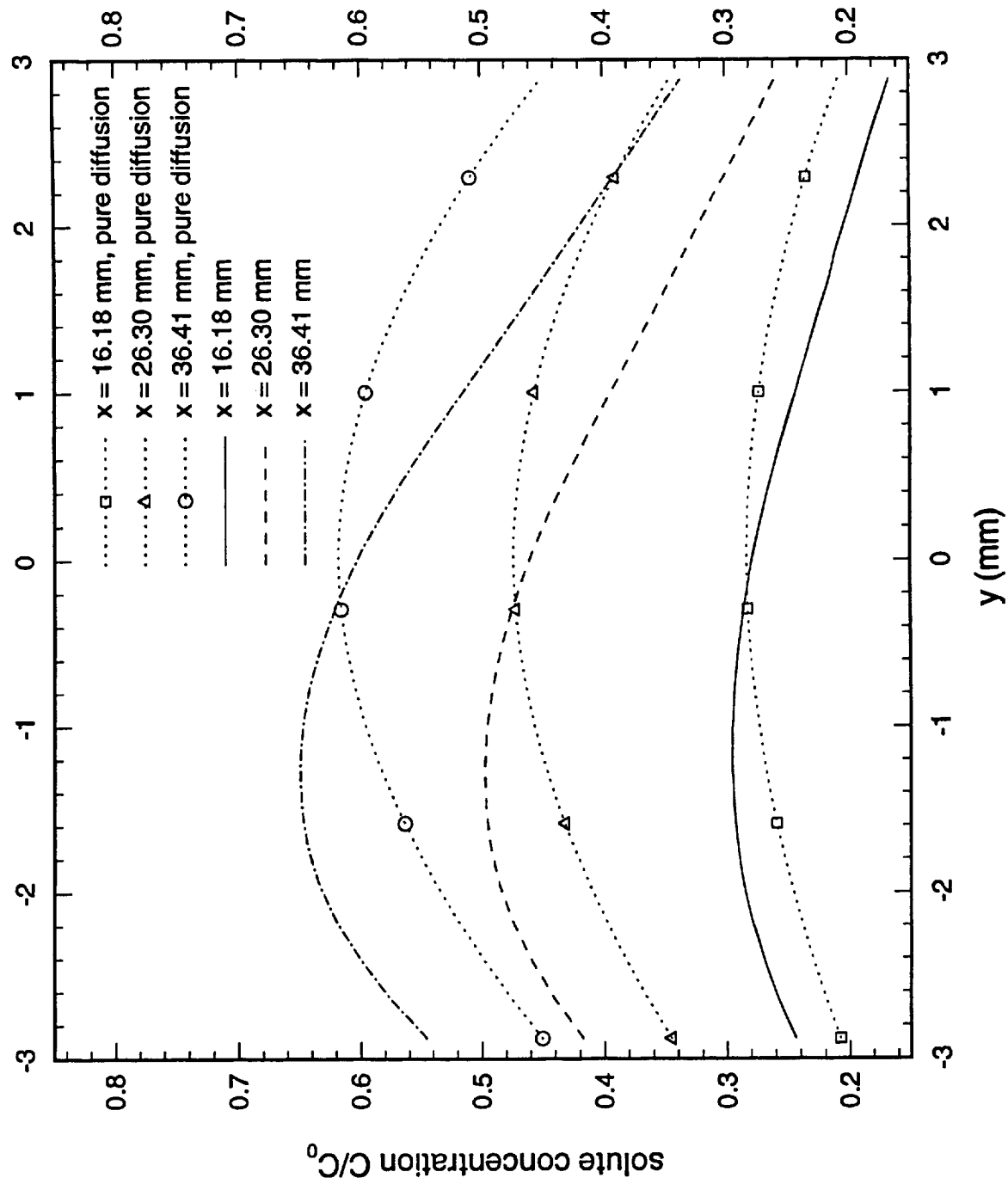

Simpson et al. Fig. 3

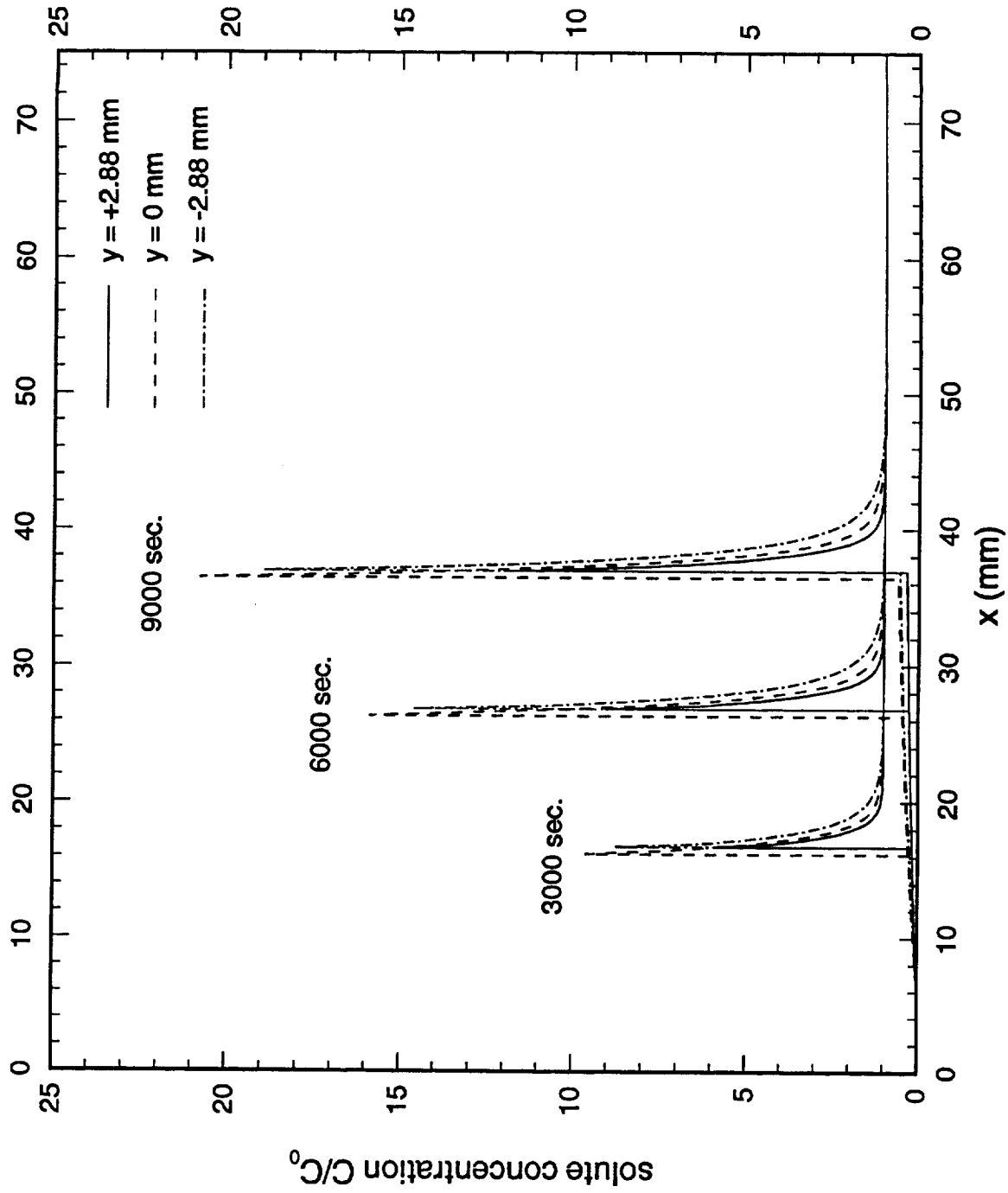

Simpson et al. Fig. 4

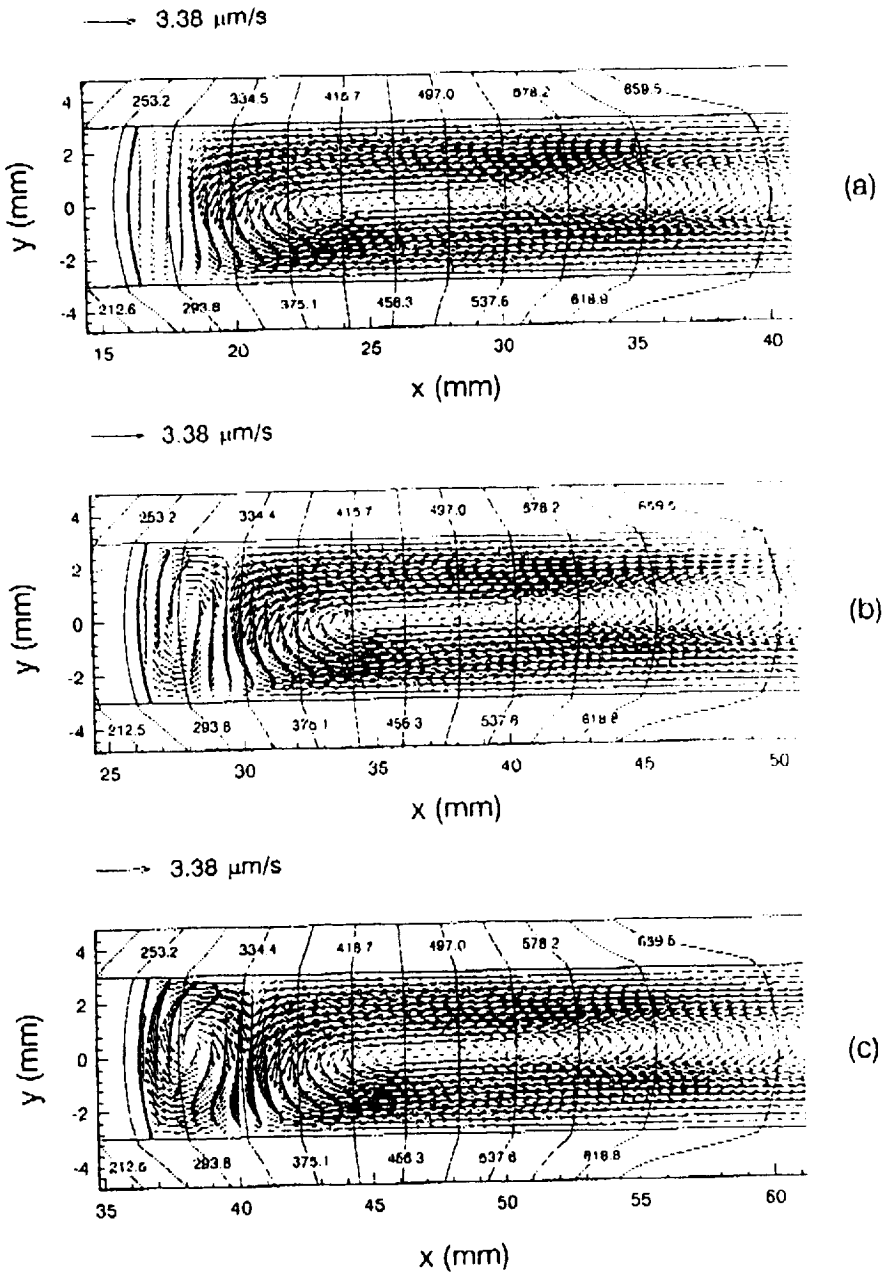

Simpson et al. Fig. 5

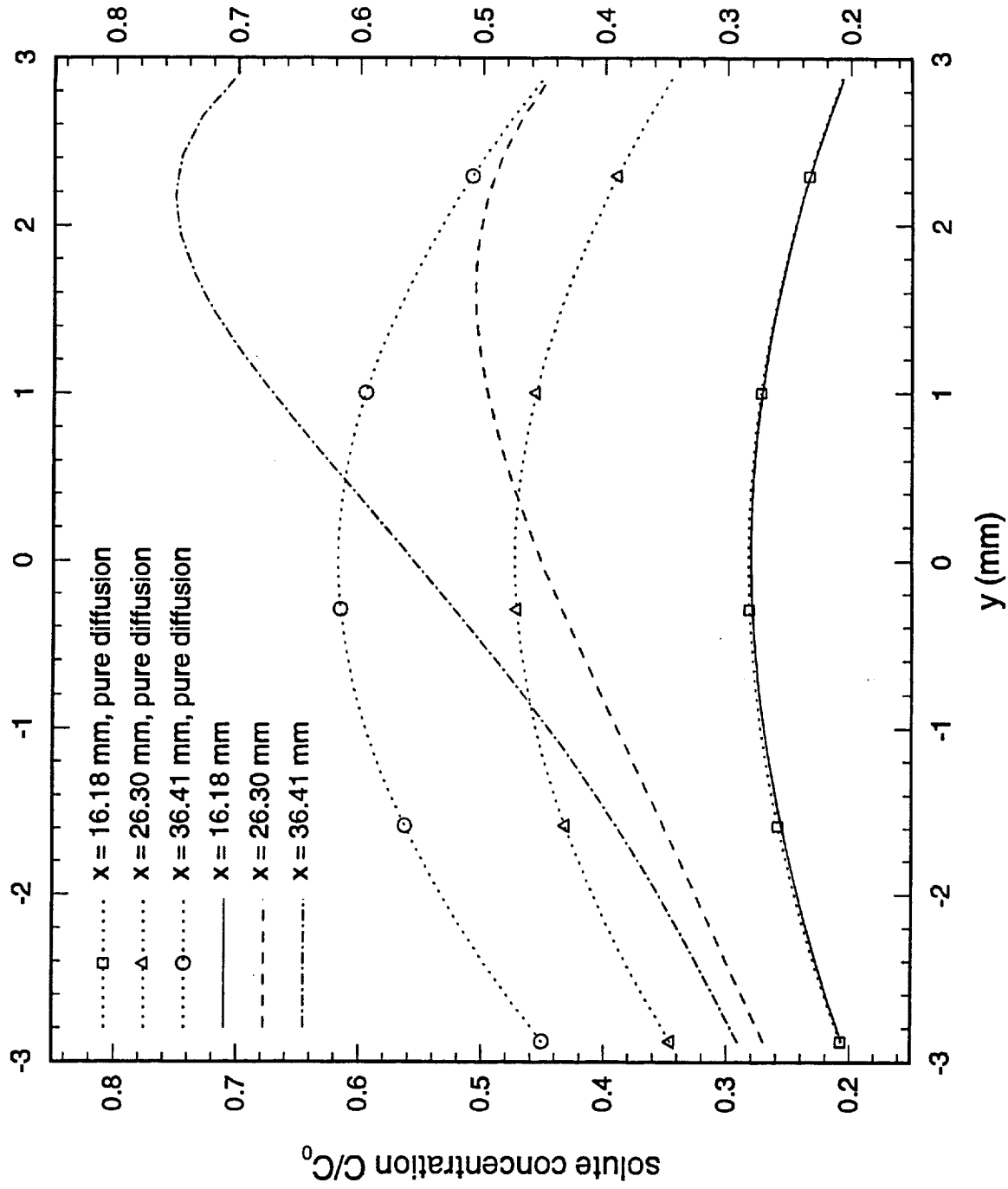

Simpson et al. Fig. 6

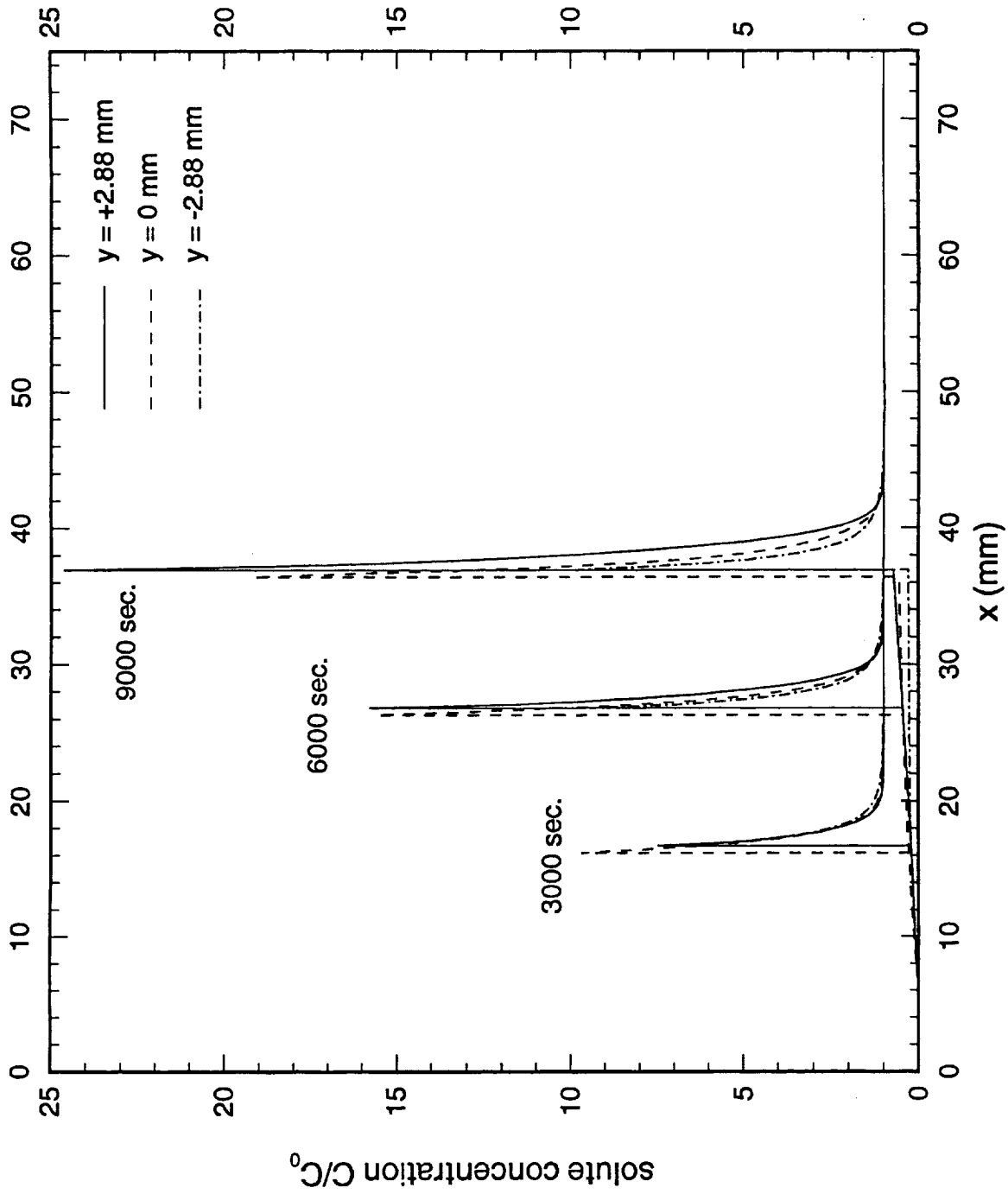

Simpson et al. Fig. 7

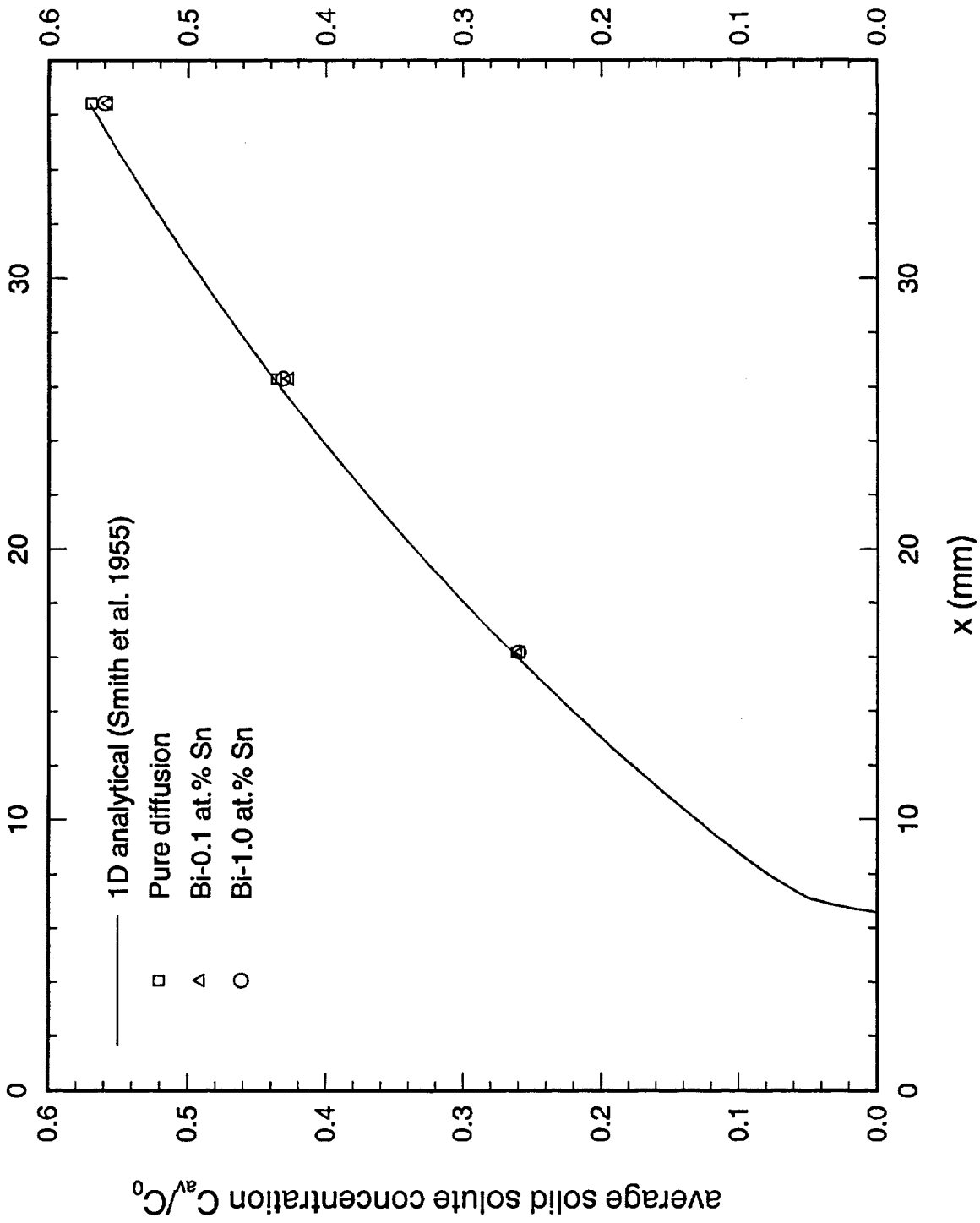

Simpson et al. Fig. 8

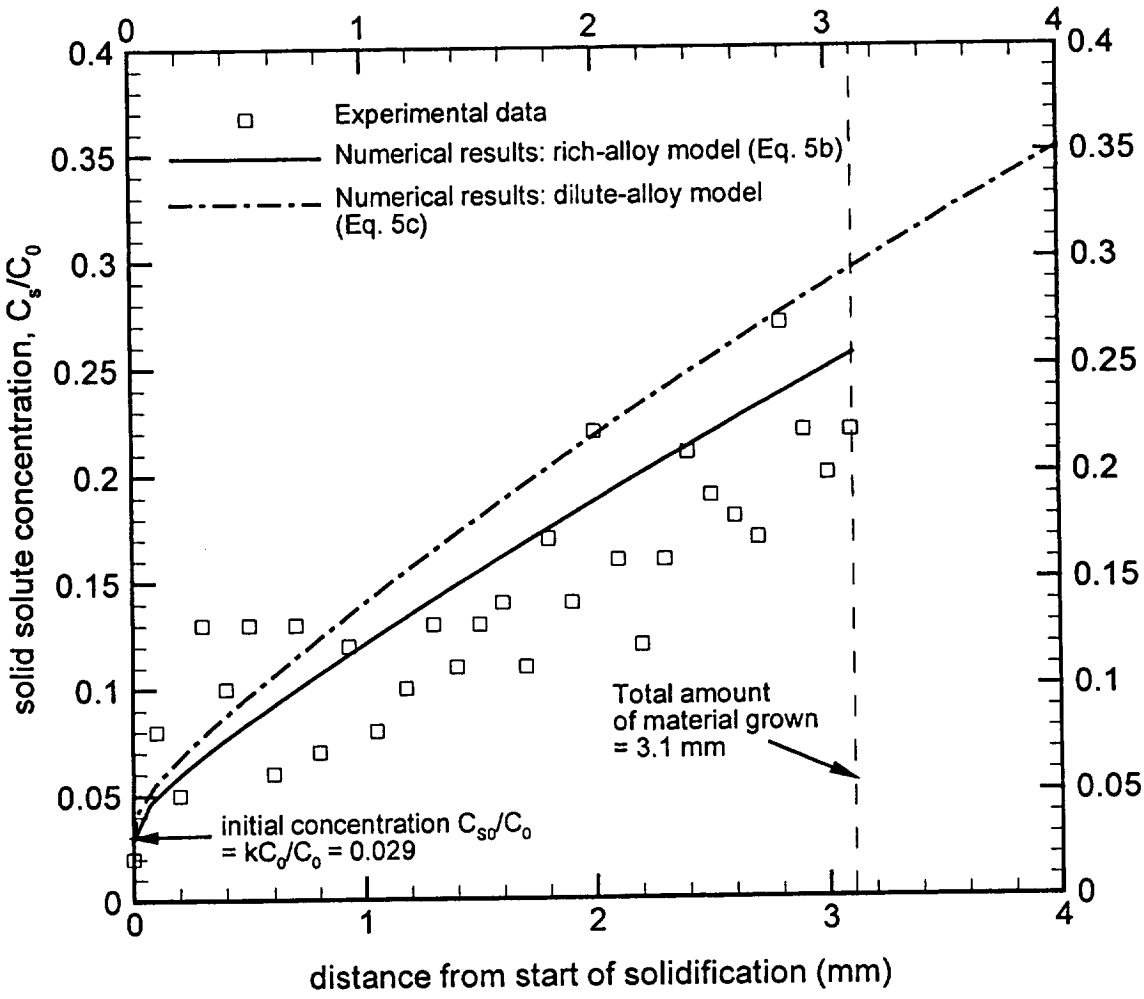

Simpson et al. Fig. 9